Biosensors and Bioelectronics 179 (2021) 113066

Contents lists available at ScienceDirect

Biosensors and Bioelectronics

journal homepage: http://www.elsevier.com/locate/bios

An ultrasensitive biosensor for dual-specific DNA based on deposition of polyaniline on a self-assembled multi-functional DNA hexahedral-nanostructure

Haohan Chen [a], Youhe Xiang [a], Rongfeng Cai [a], Liang Zhang [b,**], Yuting Zhang [a], Nandi Zhou [a,*]

[a] The Key Laboratory of Carbohydrate Chemistry and Biotechnology, Ministry of Education, School of Biotechnology, Jiangnan University, Wuxi, 214122, China
[b] National Engineering Laboratory for Cereal Fermentation Technology, Jiangnan University, Wuxi, 214122, China

ARTICLE INFO

Keywords:
Electrochemical biosensor
DNA nanostructure
G-quadruplex-hemin complex
Polyadenine
Polyaniline

ABSTRACT

Kras and Braf are major oncogenes. The mutation of Kras codon 12 or Braf V600E can lead to ovarian carcinoma. The detection of oncogene-related DNAs and their mutations offers solution for early diagnosis of ovarian cancer. Herein, a size-tunable multi-functional DNA hexahedral-nanostructure (DHN) has been rationally designed and modified on the electrode to response to Kras and Braf DNA. The size of DHN is controlled via polyadenines (polyA). The complete self-assembly of DHN depends on the presence of both target DNAs and two assistant probes. Meanwhile, a HRP-mimicking DNAzyme forms in DHN, which catalyzes the polymerization of aniline. The produced polyaniline is utilized as the output signal through differential pulse voltammetry (DPV). The biosensor shows the linear range from 100 fM to 1 μM, with the detection limit of 48.7 fM for Kras gene; and the linear range from 100 fM to 100 nM, with the detection limit of 44.1 fM for Braf gene, respectively. Since the current response depends on both gene sequences, the high specificity of the biosensor endows it to operate in an "OR"-type logic gate to discriminate the mutation of both genes. When Kras codon 12 or Braf V600E mutation happens, the response decreases significantly due to the incomplete formation of DNAzyme in DHN. The practicability of the biosensor has been verified through challenging human serum samples. Thus, it has great potential for clinical diagnosis of ovarian cancer through simultaneous detection of Kras and Braf genes and their mutations.

1. Introduction

Ovarian cancer is the leading cause of death in women who suffer from gynecologic cancer (Siegel et al., 2019). Of the various histologic subtypes of ovarian cancer, ovarian serous carcinoma is the most common and corresponds to what is generally referred to as ovarian cancer (Hsu et al., 2004). Early diagnosis of ovarian cancer is important for patients, but so far there are no effective methods (Hayashi et al., 2014). The Ras/Raf/MEK (mitogen-activated protein kinase/ERK kinase)/ERK (extracellular-signal-regulated kinase) pathway is at the center of signaling networks that governs proliferation, differentiation and cell survival. Although the basic regulatory steps have been elucidated, many features of this pathway are only beginning to emerge (Kolch, 2000). Tumors can release circulating tumor cell (CTC) and circulating tumor DNAs (ctDNA) to blood, which have been widely employed as biomarkers for tumors. ctDNA is single-strand or double-strand tumor-derived fragmented DNA, such as Kras DNA and Braf DNA. The analysis of ctDNA can provide reference information for tumor cell development (Gorgannezhad et al., 2018). Recent researches show that the most frequent genetic abnormalities in ovarian carcinoma are mutations in Kras gene and Braf gene (Nakayama et al., 2006; Singer et al., 2003). The majority mutation of Kras is located at codon 12 and all Braf mutations are at codon 600 (Davies et al., 2002; Liu et al., 2018; Mayr et al., 2006). Braf and Kras mutations are rarely both present in the same tumor, but the tumor types showing mutations of Kras or Braf are identical (Mayr et al., 2006; Nakayama et al., 2008). Therefore, the detection of Kras and Braf mutations at low concentrations can be used as a standard to determine whether ovarian cancer has occurred, *i.e.* to be utilized in cancer prognosis. So far, different biosensors have been reported for electrochemical (Zeng et al., 2019; Koo and Trau, 2020),

* Corresponding author.
** Corresponding author.
E-mail addresses: zhangl@jiangnan.edu.cn (L. Zhang), zhounandi@jiangnan.edu.cn (N. Zhou).

https://doi.org/10.1016/j.bios.2021.113066
Received 14 December 2020; Received in revised form 29 January 2021; Accepted 31 January 2021
Available online 5 February 2021
0956-5663/© 2021 Elsevier B.V. All rights reserved.

fluorescent (Li et al., 2019) and electrochemiluminescent (Zhang et al., 2017; Liu et al., 2019) detection of Kras and Braf DNAs.

Besides acting as genetic substance, DNA is a remarkable biomolecule to be used in electroanalytical chemistry (Palecek and Bartosik, 2012). Due to its self-assembled structure based on complementary base pairing, DNA has been used in a variety of electrochemical applications. To date, electrochemical biosensors based on DNA nanostructure have been applied to detect various targets, such as cell (Sun et al., 2018), heavy metal ion (Ma et al., 2018) and circulating tumor DNA (Wang et al., 2018). In the construction of biosensors, different DNA nanostructures with diverse functions, such as DNA tetrahedron (Liu et al., 2015; Wang et al., 2017), DNA nanotweezer-based nanoreactor (Liu et al., 2013), and controllable nanoscale robotic arm (Kopperger et al., 2018), have been designed and configured. In configuration of DNA sensors, the formation of Au–S bond between the thiol group modified at 3′ or 5' end of the capture probe and the gold surface is the major approach to immobilize capture probes (Wang et al., 2018). While polyadenines (polyA) composed of continuous adenine nucleotides is able to be adsorbed on the gold surface, which is comparable to Au–S bond (Pei et al., 2012; Schreiner et al., 2010). By simply adjusting the length of the polyA block, the lateral spacing and surface density of DNA on gold surface can be systematically changed. Different lengths of polyA and gold electrodes have different adsorption capacities. Previous researches have substantiated that 30-mer polyA is the optimal length for the adsorption on gold surface (Chen et al., 2017; Wang et al., 2019a). So far, various biosensors based on polyA have been constructed, and achieved satisfactory results (Liang et al., 2020; Wang et al., 2019b).

Polyaniline (PANI) is one of the most attractive conducting polymers in the field of electrocatalysis and electrochemical sensors, due to its environmental stability, redox properties and simple chemistry reactions (Amano et al., 1994; Su et al., 2017). Fortunately, DNA phosphate skeleton with large amount of negative charge, are an excellent platform for deposition of aniline (Wang et al., 2013, 2014b). Horseradish peroxidase (HRP) can catalyze the oxidative polymerization of aniline to PANI and its deposition on DNA in the presence of H_2O_2 with high controllability and high efficiency (Ge et al., 2016). DNAzymes with specific catalytic activities have been frequently utilized to construct biosensors owing to their good stability, low cost and easy preparation (Wang et al., 2014a). Among them, G-quadruplex-hemin complex, a kind of HRP-mimicking DNAzyme, has been widely applied in electrochemical (Jing et al., 2020), colorimetric (Hoang et al., 2016) and chemiluminescent (Li et al., 2017; Qi et al., 2018) assays. Particularly, considering its nucleic acid nature, it is easier to be integrated into biosensor configuration than HRP. In the presence of H_2O_2, G-quadruplex-hemin complex can catalyze the polymerization of electrochemically inactive aniline to conductive PANI to amplify the electrochemical signal. The current response in DPV is positively correlated with the amount of PANI, and therefore can be used to quantify the concentration of the target.

Inspired by the aforementioned works, a functional hexahedral-shaped DNA nanostructure is constructed for simultaneously detection of Kras gene and Braf gene. Although DHN is not as rigid as the widely used DNA tetrahedral structure, it has more spatial variability which can be used to integrate diverse designs and achieve multiple functions. The DHN is immobilized on the gold electrode through a self-assembled DHN framework consisted of four computer simulated single-stranded DNA probes (H1, H2, H3 and H4), each of which containing 30-mer polyA. The coexistence of target DNAs and assistant probes (A1 and A2) helps the formation of a complete DHN with a build-in G-quadruplex-hemin complex, which can catalyze the oxidative deposition of PANI and generate intensive electrochemical signal. The rationally designed DNA nanostructure can detect Kras gene and Braf gene either in separate mode or in simultaneous mode.

2. Experiments

2.1. Materials and reagents

All DNA sequence was synthesized and purified by Sangon Biotech Co., Ltd (Shanghai, China, https://www.sangon.com), and dissolved in TE solution to 10 μM. The sequences were shown in Table S1. 6-mercaptohexanol (6-MCH) and aniline was obtained from Sigma-Aldrich Ltd (Shanghai, China, https://www.sigmaaldrich.com). Gelred nucleic acid gel stain was purchased from Biotium Inc (California, USA, https://biotium.com). Instant premixed granules of PBS (pH 7.4) were purchased from Sinophram Chemical Reagent Co., Ltd (Shanghai, China, https://www.sinoreagent.com/). All other reagent was from Sinophram Chemical Reagent Co., Ltd. Ultrapure water with a resistivity of 18.2 MΩ cm obtained from the microporous filtration system (Billerica, USA, https://www.merckmillipore.com) was used to prepare the solution.

2.2. Self-assembly of DHN framework

Prior the formation of DHN during target detection, a DHN framework was firstly designed and immobilized on the electrode surface. The DHN framework is composed of four single-stranded probes H1, H2, H3 and H4, which were designed through NUPACK (http://www.nupack.org/) and INTEGRATED DNA TECHNOLOGIES (IDT, https://sg.idtdna.com/pages). Equimolar H1, H2, H3 and H4 were mixed with 0.1 M PBS containing 13 mM Mg^{2+} to the final concentration of 1 μM, then heated at 95 °C for 5 min, and gradually cooled down to room temperature over 30 min. The DHN framework was thus obtained through self-assembly.

2.3. Preparation and modification of Au electrode

The Au electrode (AuE) was immersed in Piranha solution (H_2SO_4:30% H_2O_2 = 7:3) for 15 min and polished with 0.05 μm Al_2O_3 suspension for 3 min, and then sonicated in ultrapure water for 3 min and gently dried with nitrogen. 5 μL self-assembled DHN framework was dropped on AuE and incubated for 12 h at 30 °C in a constant temperature incubator. The DHN framework was thus constructed on the AuE surface via polyA-Au interaction. Then, the AuE was rinsed with 0.1 M PBS and dried with nitrogen gently to remove unexpected binding. The AuE was further incubated with 2 mM 6-MCH for 1 h at 37 °C to block non-specific binding sites. Subsequently, the electrode was rinsed with 0.1 M PBS thoroughly and dried with nitrogen. Thus the DHN framework modified AuE was obtained.

2.4. Formation of HRP-mimicking DNAzyme and catalytic deposition of PANI

5 μL sample containing target DNAs was dropped on the above prepared DHN framework modified AuE, and incubated at 37 °C for 1 h. After rinsing with PBS, 5 μL equimolar assistant probes (A1 and A2) was dropped on the electrode surface and incubated at 37 °C for 1 h, followed by thorough rinsing with 0.1 M PBS and dried with nitrogen. Next, the AuE was immersed into G-quadruplex forming solution (10 mM HEPES, 50 mM KCl, pH 8.0) containing 200 μM hemin for 1 h at 37 °C, then washed with 0.1 M PBS and gently dried with nitrogen. The HRP-mimicking DNAzyme was thus formed. For the deposition of PANI, the electrode was incubated in deposition buffer (0.1 M HAc-NaAc, pH 4.3, containing 100 mM aniline, 100 mM H_2O_2) at 30 °C for 90 min.

2.5. Electrochemical measurements

All electrochemical measurements were executed with CHI 660 E electrochemical workstation (Shanghai Chenhua Equipments, China, http://www.chinstr.com/). A three electrode system was consisted of a platinum electrode as counter electrode, Ag/AgCl electrode as reference

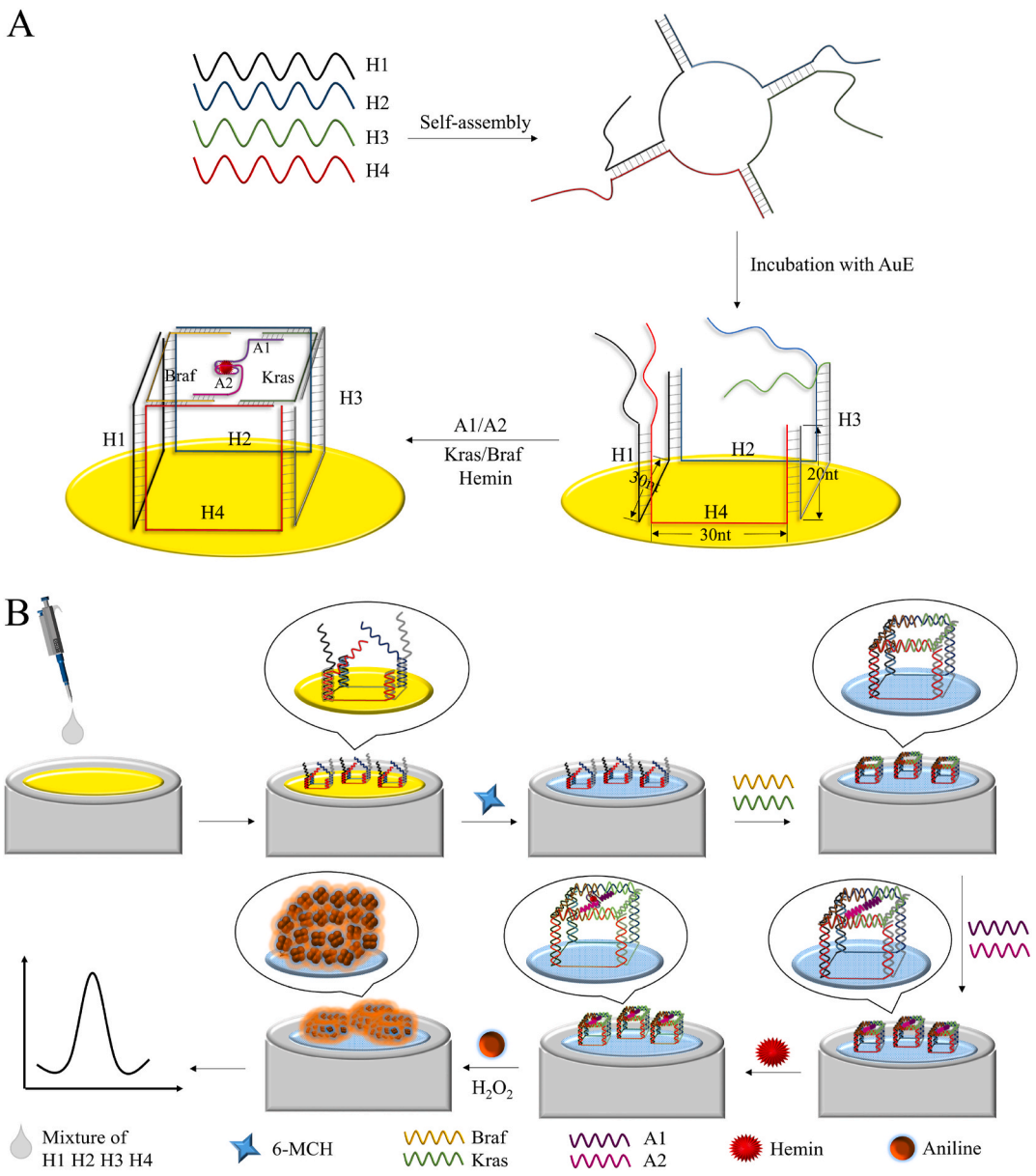

Scheme 1. (A) The simplified diagram of the self-assembly of single-stranded probes, target DNAs and assistant probes to DHN nanostructure; (B) Schematic illustration of the proposed electrochemical biosensor for Kras and Braf gene.

electrode, and 3 mm diameter modified AuE as working electrode.

Electrochemical impedance spectroscopy (EIS) was performed in 0.1 M KCl containing 1 mM $[Fe(CN)_6]^{4-/3-}$ with a frequency range from 0.1 Hz to 10 kHz. Cyclic voltammetry (CV) was carried out in 0.1 M HAc-NaAc, scanning from −0.3 V to 0.3 V. Different pulse voltammetry (DPV) was also performed in 0.1 M HAc-NaAc, the potential range was from −0.2 V to 0.2 V, with the increasement of 0.004 V, amplitude of 0.05 V, and pulse width of 0.05 s.

3. Results and discussion

3.1. Designed strategy for the electrochemical biosensor

The schematic illustration of the construction and detection principle of the biosensor is shown in Scheme 1. Scheme 1A shows a brief description of the self-assembly of the DHN framework, and the completely formation of the DHN nanostructure after hybridization with the target DNAs and assistant probes. The rational designed H1, H2, H3 and H4 have 20 complementary bases according to the principle of Watson-crick base pairing, making up the height of the DHN framework. After the mixture of H1, H2, H3 and H4 was dropped on the AuE, 30-mer polyA can specifically adsorb on the electrode surface, which constitutes the bottom of the DHN framework. Kras and Braf gene sequences can hybridize with the hanging single-stranded DNA (ssDNA) regions at the top of the DHN framework and fix the loose hanging ssDNAs, so that the entire DNA nanostructure becomes a hexahedral shape with the height of 20 oligonucleotides (nt) and the length and width of 30 nt. Meanwhile, at the 3′ and 5′ ends of Kras DNA and Braf DNA, 8 nt are left for complementary with A1 and A2 respectively. After incubation with the assistant probes and subsequent the G-quadruplex forming solution containing hemin, G-quadruplex-hemin complex with HRP-mimicking activity can be formed. The DHN can be designed in size-tunable mode according to the length of the target sequences. However, the variation in the size of DHN may lead to change in the amount of the produced PANI and subsequent the intensity of the output signal due to the adjusted duplex regions. And the binding strength with the gold

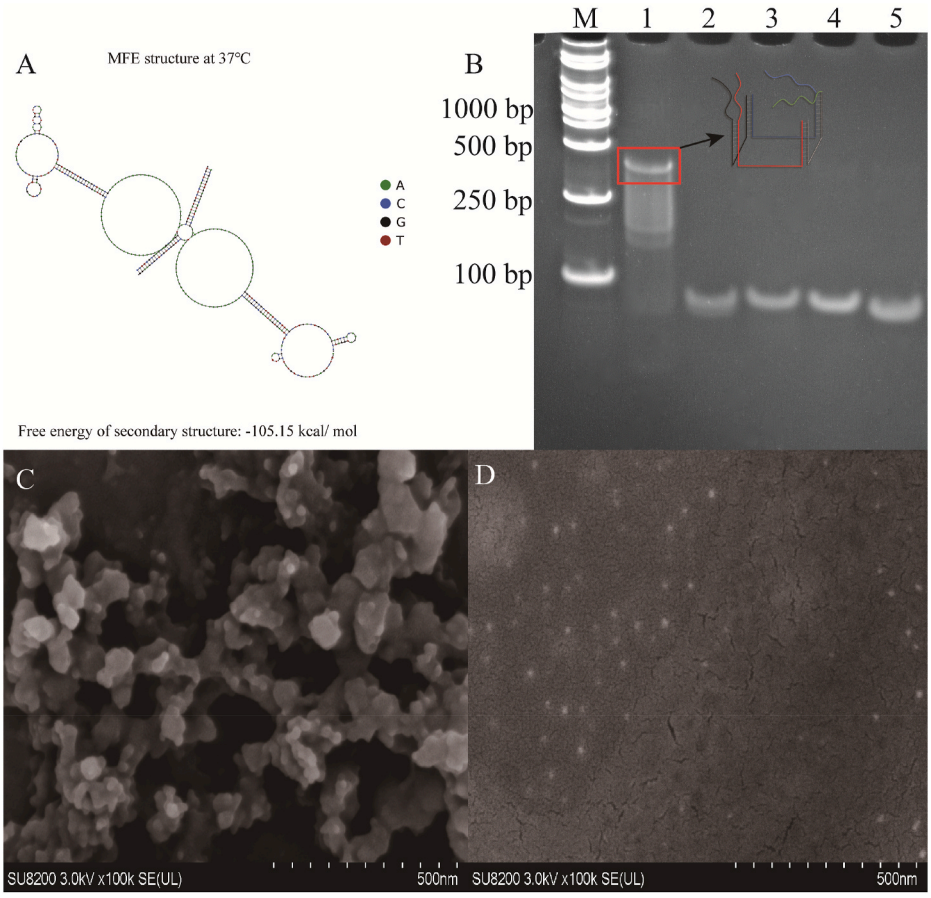

Fig. 1. (A) The simulation results of the designed DHN framework. The double-stranded regions are four heights of the DHN framework, the single-stranded polyA consists the bottom of DHN framework; (B) PAGE analysis. Lane M: DL 5000 marker; Lane 1: the mixture of 1 μM H1, H2, H3 and H4; Lane 2: 1 μM H1; Lane 3: 1 μM H2; Lane 4: 1 μM H3; Lane 5: 1 μM H4; (C) SEM image of PANI deposition on the gold substrate with DHN. The scale bar indicates 500 nm; (D) SEM image of gold substrate before PANI deposition. The scale bar indicates 500 nM. (For interpretation of the references to color in this figure legend, the reader is referred to the Web version of this article.)

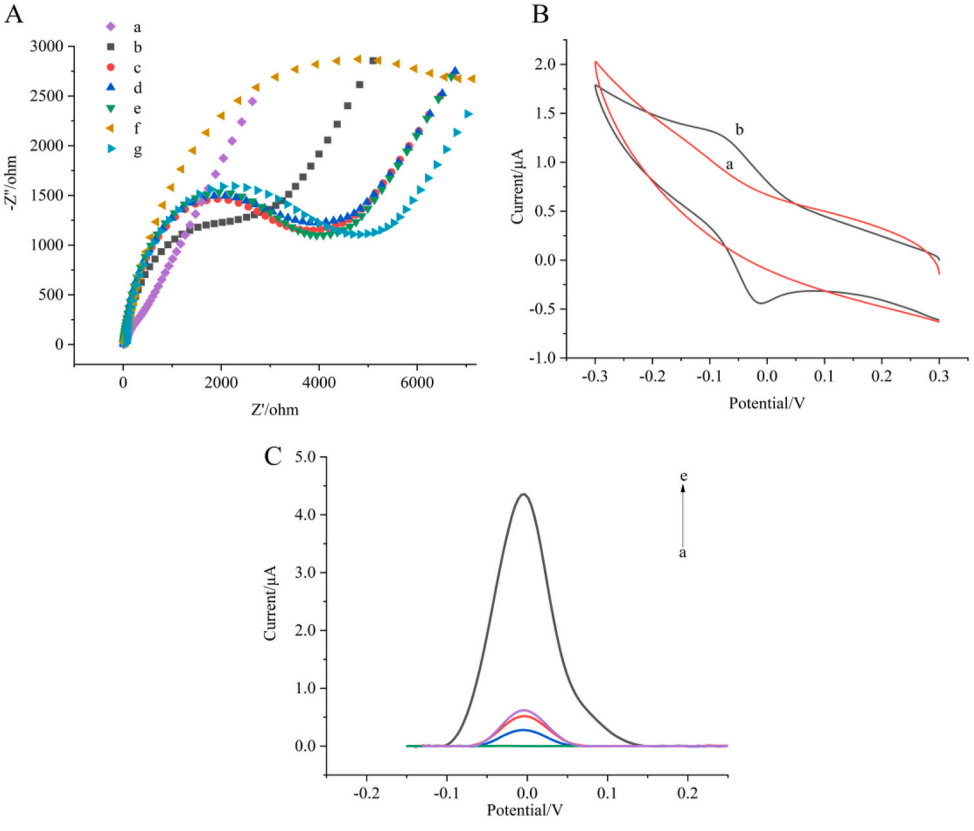

Fig. 2. (A) EIS characterization of the electrode modification: (a) bare AuE; (b) AuE/DHN framework; (c) AuE/DHN framework/MCH; (d) AuE/DHN framework/MCH/Kras&Braf; (e) AuE/DHN framework/MCH/Kras&Braf/A1&A2; (f) AuE/DHN framework/MCH/Kras&Braf/A1&A2/G-quadruplex-hemin; (g) AuE/DHN framework/MCH/Kras&Braf/A1&A2/G-quadruplex-hemin/PANI; (B) CV responses of (a) bare AuE; (b) AuE/DHN framework/MCH/Kras&Braf/A1&A2/PANI. (C) DPV responses of different electrodes with PANI deposition (a) AuE; (b) AuE/DHN framework/MCH/A1&A2; (c) AuE/DHN framework/MCH/Braf/A1&A2; (d) AuE/DHN framework/MCH/Kras/A1&A2; (e) AuE/DHN framework/MCH/Kras&Braf/A1&A2.

electrode and the rigidity of the structure will also be changed. As shown in Scheme 1B, the formed HRP-mimicking DHN catalyzes the deposition of PANI on DNA phosphate skeletons in the presence of H_2O_2 and aniline. By conducting DPV scanning, a current signal of PANI can be recorded. The current response is dependent on the amount of G-quadruplex-hemin complex, which is linearly related to the concentration of the target sequences. When mutations of Braf V600E or codon 12 of Kras occur, the hybridization of the assistant probes with the target DNAs and subsequent formation of G-quadruplex-hemin complex are hindered, and thus the current response is intensively reduced.

3.2. Feasibility study of the electrochemical biosensor

Fig. 1A shows the secondary structure docking diagram of the DHN framework simulated by NUPACK. The double-stranded regions are the four heights of the DHN framework, while the single-stranded polyA regions construct the bottom of DHN framework which adsorbs on the AuE surface. The loose structures on both sides are the hanging ssDNAs, which are the complementary region of Kras and Braf. The simulation diagram illustrates that the designed H1, H2, H3 and H4 can form the expected spatial structure.

In order to verify the formation of the expected DNA structure in the experiment, polyacrylamide gel electrophoresis (PAGE) was carried out, and the electrophoresis image is shown in Fig. 1B. Lane 1 is 1 μM mixture of H1, H2, H3 and H4. A clear band represents the expected DHN nanostructure can be observed.

The surface morphology of the synthesized PANI on the gold substrate was characterized by scanning electron microscope (SEM) (Fig. 1C). Compared with the gold substrate with only DHN framework on the surface (Fig. 1D), the formation of PANI can be clearly revealed.

The modification process on the surface of AuE was characterized by EIS. Since the electroactive species in the solution are repelled by the negative charge of the DNA phosphate skeleton to approach the electrode surface, the diameter of the semicircle in EIS curve increases, which means the increase of electron transfer resistance (R_{et}). As shown in Fig. 2A, bare AuE (curve a) shows an almost linear curve, indicating that the neglected R_{et} between the electroactive $[Fe(CN)_6]^{3-/4-}$ and the electrode. After the modification of the DHN framework on the AuE (curve b), the R_{et} of the electrode apparently increases. After blocking with 6-MCH (curve c), the R_{et} value apparently increases, since 6-MCH fully blocks the vacant sites on the electrode and restricts the approaching of $[Fe(CN)_6]^{3-/4-}$ to the electrode surface. After the introduction of Kras/Braf DNA (curve d) and subsequent assistant probes (curve e), R_{et} further increases owing to the increased coverage of DNA skeleton on the electrode. With the formation of G-quadruplex intercalated with hemin (curve f), the R_{et} increases dramatically due to the repulsion between $[Fe(CN)_6]^{3-/4-}$ and negative-charged G-quadruplex. However, the R_{et} decreases obviously after the deposition of PANI (curve g). This can be ascribed to the excellent conductivity of PANI, which accelerates the electron transfer.

CV and DPV measurements were also employed to verify the principle of the biosensor. CV curves in Fig. 2B indicate the typical redox response of PANI in 0.1 M HAc-NaAc. No peak can be observed at bare AuE (curve a), while a pair of redox peaks appear at −0.04 V and 0.00 V after deposition of PANI (curve b). Fig. 2C shows DPV curves recorded under different conditions. No current response can be observed in bare AuE (curve a). Curve b is the blank experiment from the DHN framework-modified electrode, which shows weak DPV response. While Braf DNA (curve c) or Kras DNA (curve d) is introduced individually to the DHN framework, the current response is only slightly higher than that of curve b. Assistant probes cannot form HRP-mimicking enzyme without target sequences, leading to almost no increase in DPV response. However, an obvious DPV current peak can be obtained when both Kras and Braf are introduced, because the assistant probes can combine with Kras and Braf DNA to form the complete DHN with HRP-mimicking activity, leading to the deposition of a great number of PANI on DNA phosphate skeleton.

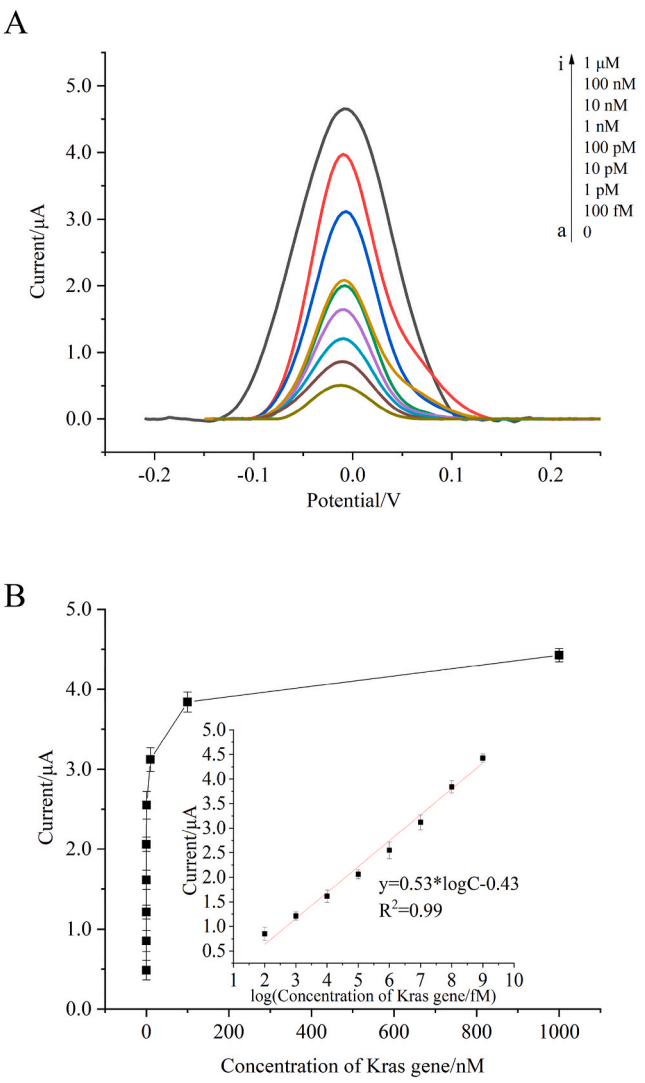

Fig. 3. (A) DPV curves recorded at 1 μM Braf and different concentration of Kras gene (a) 0 M; (b) 100 fM; (c) 1 pM; (d) 10 pM; (e) 100 pM; (f) 1 nM; (g) 10 nM; (h) 100 nM; (i) 1 μM. (B) The relationship between the peak current in DPV and the concentration of Kras DNA. The insert shows the corresponding calibration plot for the peak current vs. logarithm Kras gene concentration in the range from 100 fM to 1 μM.

3.3. Optimization of experimental conditions

To obtain the optimal performance of the DHN-based biosensor, the experimental conditions were investigated. The performance of the DHN-based biosensor was optimized from four factors: (1) concentration of DHN-forming single-stranded probes, (2) concentration of assistant probes, (3) concentration of H_2O_2, and (4) deposition time of PANI (Fig. S1).

DHN framework is formed through self-assembly of equimolar single-stranded probes H1, H2, H3 and H4. The concentration of DHN framework depends on the concentration of single-stranded probes, and determines the amount of the capture sites for target DNAs. According to the results in Fig. S1A, the peak current in DPV gradually increases with the increased concentration of single-stranded probes from 150 nM to 300 nM. However the current decreases when the concentration of the probes exceeds 300 nM, which may be ascribed to the steric hindrance of the DNA three-dimensional structure. Thus the optimal concentration of the single-stranded probes is 300 nM. The concentration of assistant

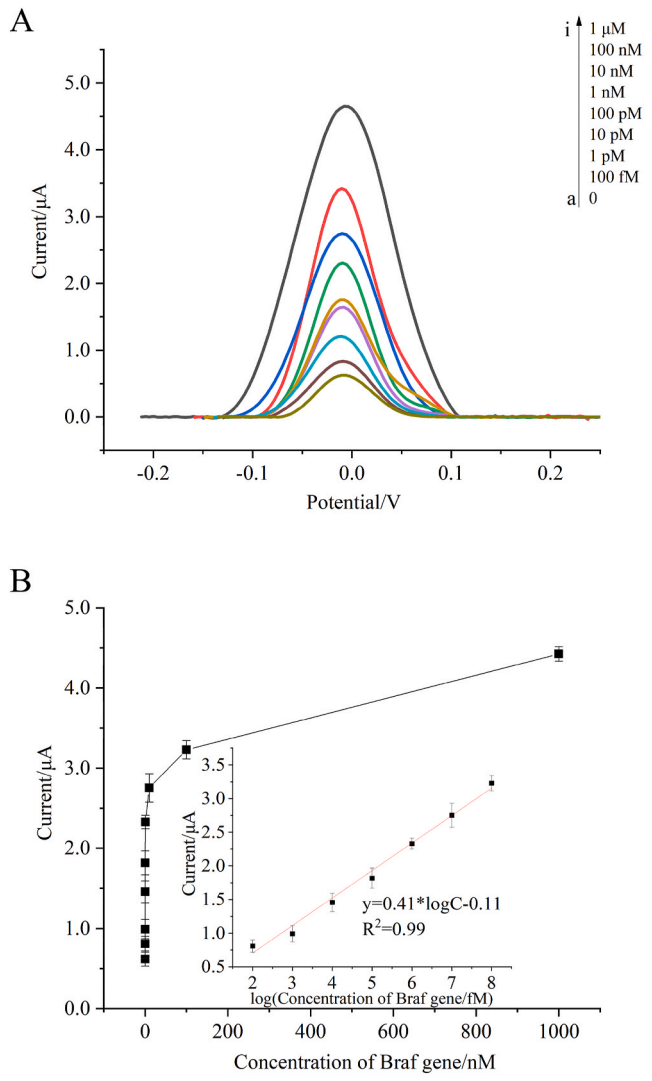

Fig. 4. (A) DPV response for 1 μM Kras and different concentration of Braf gene (a) 0 M; (b) 100 fM; (c) 1 pM; (d) 10 pM; (e) 100 pM; (f) 1 nM; (g) 10 nM; (h) 100 nM; (i) 1 μM. (B) The relationship between the peak current in DPV and the concentration of Braf DNA. The insert shows the corresponding calibration plot for the peak current vs. logarithm Braf gene concentration in the range from 100 fM to 100 nM.

probes affects the formation of HRP-mimicking DNAzyme, and subsequently determines the polymerization efficiency of PANI. Fig. S1B reveals that the highest peak current in DPV appears when the concentration of the assistant probes reaches 100 nM H_2O_2 acts as an oxidant in the deposition of PANI, so the concentration of H_2O_2 was optimized. Fig. S1C shows that current response increases with the increased concentration of H_2O_2 in the range from 60 mM to 100 mM, and then levels off. Thus the optimal concentration of H_2O_2 is 100 mM. The effect of the deposition time of PANI is shown in Fig. S1D. The DPV response obviously increases with the extended reaction time and reaches the highest in 90 min. Thus 90 min is the optimal deposition time.

3.4. Analytical performance of the biosensor

According to the design diagram, the DHN-based biosensor can be used to detect both Kras and Braf gene sequences. To detect one gene sequence of Kras/Braf, the other sequence needs to be added to the reaction system at a fixed concentration of 1 μM, and thus the DPV response is correlated to the concentration of the target sequence. All detections were carried out under the optimal experimental conditions.

Table 1
Detection of target DNA sequences in human serum samples.

Added	Found	Recovery (%)	RSD (%)
50 nM	54.2 nM	108.40	2.13
70 pM	68.5 pM	97.86	3.43
80 fM	86.5 fM	108.13	5.96

The calibration curve for Kras gene was firstly plotted. Fig. 3A indicates the DPV curves recorded at different concentration of Kras gene sequence. The DPV response increases with the elevated concentration of Kras gene. Fig. 3B depicts the relationship between the peak current in DPV and the concentration of Kras gene. In the concentration range from 10^2 fM to 10^9 fM, a linear relationship between the peak current and the logarithm of the concentration can be derived, with the regression equation of $y = 0.53*\log C - 0.43$ ($R^2 = 0.99$), where y and C represent the peak current (μA) and the concentration of target DNA (fM). The limit of detection (LOD) is 48.7 fM (LOD = 3 S/N).

Similarly, the calibration curve for Braf gene was plotted by fixing the concentration of Kras gene sequence while changing the concentration of Braf gene sequence. As shown in Fig. 4, when the concentration of Braf increases, the current response increases gradually. A linear relationship between the peak current and the logarithm of the concentration of Braf is also derived in the range from 10^2 fM to 10^8 fM. The regression equation is $y = 0.41*\log C - 0.11$ ($R^2 = 0.99$), with the detection of limit of 44.1 fM. These results suggest that the proposed biosensor shows high sensitivity for both target DNAs.

To further investigate the repeatability of the electrochemical biosensor, six electrodes were separately modified and used to detect the samples with 100 pM of Kras and Braf. With the average detection value of 99.53 pM and RSD of 4.39%, the electrochemical biosensor has good repeatability.

In order to verify selectivity of the electrochemical biosensor in the presence of other interference gene sequences, 1 μM mixture of Nras, Pax-5a and KIT gene sequences were added to the detection system together with the target DNAs, and the DPV current responses in the absence and presence of interferents were compared. As shown in Fig. S2, the current responses hardly change when the interference gene sequences are introduced, which proves the good interferent-resistance of the proposed electrochemical biosensor.

To further explore the practicability of the biosensor in clinical

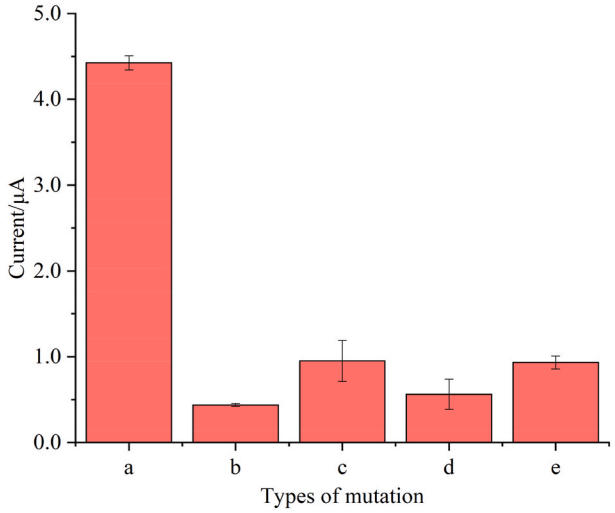

Fig. 5. DPV responses to different types of mutations for Kras and Braf gene sequences: (a) wild type Kras and Braf; (b) Kras mutation type 1 and wild Braf; (c) Kras mutation type 2 and wild Braf; (d) Kras mutation type 3 and wild Braf; (e) wild type Kras and Braf V600E. The concentration of each sequence was fixed at 1 μM.

samples, recovery tests were conducted. Human serum serves as the complex biological system. Equimolar standard Kras and Braf DNA sequences were spiked into human serum to prepare a series of serum samples with determined concentration of target DNAs. And the samples were detected with dilution. As shown in Table 1, the recoveries of the target sequences range from 97.86% to 108.40%, with the RSD varying from 2.13% to 5.96%. These results indicate that the sensor has good interferent-resistance in complex sample matrix and has great potential to be applied to actual sample detection.

Durability is also an important feature of the biosensor in practical application. The durability of the biosensor was evaluated by storing the modified electrode at 4 °C and measuring the DPV response every two days. As shown in Fig. S3, 88.41% of the original current signal was recovered after the electrode was stored for 14 days.

3.5. Discrimination of the mutation of the gene sequences

The biosensor is designed to be able to discriminate the mutation of either Kras or Braf gene sequences simultaneously for clinical diagnosis. The mutation of either Kras codon 12 or Braf V600E suggests that ovarian carcinoma may happen. Therefore, high sequence-specificity of the biosensor is critical for the diagnosis of ovarian tumors. Different combinations of wild sequences and mutant sequences were prepared and detected employing the same experimental conditions. The results are shown in Fig. 5. The sample containing the combination of wild Kras and Braf gene sequences appears high peak current in DPV curve. However, the presence of any of the three mutation type of Kras gene or the mutation of Braf (Braf V600E) leads to very low peak current. The current responses of the mutant samples are only 9.87%–21.49% of that of the wild sample. To further validate the practicability, the experiment was also performed in human serum samples. The target DNAs and mutant sequences were spiked into human serum respectively, and then diluted with 0.1 M PBS containing 13 mM Mg^{2+}. The detection was conducted just the same as the above. As shown in Fig. S4, the peak currents of the four mutant types are only 19.63%–26.75% of that of the wild type. Therefore, the constructed biosensor can easily discriminate the mutation of Kras and Braf sequences, suggesting its potential in tumor diagnosis.

4. Conclusion

In this paper, a size-tunable multi-functional DHN-based biosensor was successfully constructed for Kras and Braf dual-gene sequences through the formation of HRP-mimicking DNAzyme and its catalysis of polymerization of aniline to PANI. Taking advantage of the unique design of the DNA nanostructure with build-in catalytic activity, the proposed biosensor shows high sensitivity and wide detection range over six orders of magnitude for both gene sequences. The detection limits for the two targets are down to fM level. The interferent-resistance of the biosensor in complex matrix is validated through challenging spiked serum samples, and satisfactory recovery and RSD are obtained. Moreover, the biosensor can be utilized as an “OR”-type logic gate to discriminate the mutation happened in either Kras gene or Braf gene. Therefore, the proposed DHN-based biosensor provides a promising tool for dual-detection of the target DNAs, and has potential prospect for early diagnosis of ovarian carcinoma.

CRediT authorship contribution statement

Haohan Chen: Investigation, Data curation, Writing - original draft. **Youhe Xiang:** Investigation, Validation, Data curation. **Rongfeng Cai:** Formal analysis, Validation. **Liang Zhang:** Validation, Supervision. **Yuting Zhang:** Supervision. **Nandi Zhou:** Writing - review & editing, Supervision, Funding acquisition.

Declaration of competing interest

The authors declare that they have no known competing financial interests or personal relationships that could have appeared to influence the work reported in this paper.

Acknowledgement

This research was supported by the Six Talent Peaks Project in Jiangsu Province (JY-078).

Appendix A. Supplementary data

Supplementary data to this article can be found online at https://doi.org/10.1016/j.bios.2021.113066.

References

Amano, K., Ishikawa, H., Kobayashi, A., Satoh, M., Hasegawa, E., 1994. Synth. Met. 62, 229–232.
Chen, L., Chao, J., Qu, X., Zhang, H., Zhu, D., Su, S., Aldalbahi, A., Wang, L., Pei, H., 2017. ACS Appl. Mater. Interfaces 9, 8014–8020.
Davies, H., Bignell, G.R., Cox, C., Stephens, P., Edkins, S., Clegg, S., Teague, J., Woffendin, H., Garnett, M.J., Bottomley, W., 2002. Nature 417, 949–954.
Ge, S., Wu, K., Zhang, Y., Yan, M., Yu, J., 2016. Biosens. Bioelectron 80, 215–221.
Gorgannezhad, L., Umer, M., Islam, M.N., Nguyen, N.T., Shiddiky, M.J.A., 2018. Lab Chip 18, 1174–1196.
Hayashi, Y., Sasaki, H., Takeshita, S., Nishikawa, R., Nishikawa, H., Arakawa, A., Yamashita, Y., Takahashi, S., Sugiura-Ogasawara, M., 2014. Oncol. Rep 32, 1815–1819.
Hsu, C.Y., Cha, M.S., Ho, C.L., Wang, T.L., Bristow, R., Wang, B.G., Kurman, R.J., Shih, L. M., 2004. Clin. Cancer Res. 10, 6432–6436.
Hoang, M., Huang, P.-J.J., Liu, J., 2016. ACS Sens. 1, 137–143.
Jing, C., Chen, H., Cai, R., Tian, Y., Zhou, N., 2020. Anal. Methods 12, 3285–3289.
Kolch, W., 2000. Biochem. J. 351, 289–305.
Koo, K.M., Trau, M., 2020. ACS Sens. 5, 3217–3225.
Kopperger, E., Madhira, J.L.S., Rothfischer, F., Lamb, D.C., Simmel, F.C., 2018. Science 359, 296–301.
Li, Q., Zhou, D., Pan, J., Liu, Z., Chen, J., 2019. Analyst 144, 3088–3093.
Li, X., Zhang, H., Tang, Y., Wu, P., Xu, S., Zhang, X., 2017. ACS Sens. 2, 810–816.
Liang, X., Zhao, J., Ma, Z., 2020. Sens. Actuator B-Chem. 304, 127278.
Liu, M., Fu, J., Hejesen, C., Yang, Y., Woodbury, N.W., Gothelf, K., Liu, Y., Yan, H., 2013. Nat. Commun. 4, 2127.
Liu, R., Zhang, T., Zhu, G., Xing, M., 2018. Nat. Commun. Now. 9, 579.
Liu, S., Su, W., Li, Z., Ding, X., 2015. Biosens. Bioelectron 71, 57–61.
Liu, Y., Wang, M.K., Nie, Y.X., Qian, Z., Ma, Q., 2019. Anal. Chem. 91, 6250–6258.
Ma, R.N., Wang, L.L., Zhang, M., Jia, L.P., Zhang, W., Shang, L., Jia, W.L., Wang, H.S., 2018. Sens. Actuator B-Chem. 257, 678–684.
Mayr, D., Hirschmann, A., Lohrs, U., Diebold, J., 2006. Gynecol. Oncol. 103, 883–887.
Nakayama, K., Nakayama, N., Kurman, R.J., Cope, L., Pohl, G., Samuels, Y., Velculescu, V.E., Wang, T.L., Shih, L.M., 2006. Cancer Biol. Ther 5, 779–785.
Nakayama, N., Nakayama, K., Yeasmin, S., Ishibashi, M., Katagiri, A., Iida, K., Fukumoto, M., Miyazaki, K., 2008. Br. J. Cancer 99, 2020–2028.
Palecek, E., Bartosik, M., 2012. Chem. Rev. 112, 3427–3481.
Pei, H., Li, F., Wan, Y., Wei, M., Liu, H., Su, Y., Chen, N., Huang, Q., Fan, C., 2012. J. Am. Chem. Soc. 134, 11876–11879.
Qi, H., Yue, S., Bi, S., Song, W., Ding, C., 2018. Sens. Actuator B-Chem. 273, 1525–1531.
Schreiner, S.M., Shudy, D.F., Hatch, A.L., Opdahl, A., Whitman, L.J., Petrovykh, D.Y., 2010. Anal. Chem. 82, 2803–2810.
Siegel, R.L., Miller, K.D., Jemal, A., 2019. CA A Cancer J. Clin. 69, 7–34.
Singer, G., Oldt, R., Cohen, Y., Wang, B.G., Sidransky, D., Kurman, R.J., Shih, I.M., 2003. J. Natl. Cancer Inst. 95, 484–486.
Su, Z., Xu, X., Xu, H., Zhang, Y., Li, C., Ma, Y., Song, D., Xie, Q., 2017. Microchim. Acta 184, 1677–1682.
Sun, D., Lu, J., Luo, Z., Zhang, L., Liu, P., Chen, Z., 2018. Biosens. Bioelectron. 120, 8–14.
Wang, F., Lu, C.H., Willner, I., 2014a. Chem. Rev. 114, 2881–2941.
Wang, H.F., Ma, R.N., Sun, F., Jia, L.P., Zhang, W., Shang, L., Xue, Q.W., Jia, W.L., Wang, H.S., 2018. Biosens. Bioelectron. 122, 224–230.
Wang, L., Zhang, H., Wang, C., Xu, Y., Su, J., Wang, X., Liu, X., Feng, D., Wang, L., Zuo, X., Shi, J., Ge, Z., Fan, C., Mi, X., 2019a. Biosens. Bioelectron. 127, 85–91.
Wang, Q., Wen, Y., Li, Y., Liang, W., Li, W., Li, Y., Wu, J., Zhu, H., Zhao, K., Zhang, J., Jia, N., Deng, W., Liu, G., 2019b. Anal. Chem. 91, 9277–9283.
Wang, X., Chen, F., Zhang, D., Zhao, Y., Wei, J., Wang, L., Song, S., Fan, C., Zhao, Y., 2017. Chem. Sci. 8, 4764–4770.
Wang, Z.G., Liu, Q., Ding, B., 2014b. Chem. Mater. 26, 3364–3367.
Wang, Z.G., Zhan, P., Ding, B., 2013. ACS Nano 7, 1591–1598.
Zeng, N., Xiang, J., 2019. Talanta 198, 111–117.
Zhang, Y., Wang, L., Luo, F., Qiu, B., Guo, L., Weng, Z., Lin, Z., Chen, G., 2017. Chem. Commun. 53, 2910–2913.